

Phonons at functional oxide interfaces: An *in situ* sum-frequency spectroscopic perspective

Shiyu Zhang(张诗雨), Junjie Dong(董俊杰), Tongying Liu(刘彤影), and Wei-Tao Liu(刘韡韬)
Citation: Chin. Phys. B, 2026, 35 (**6**): 064203. DOI: 10.1088/1674-1056/ae5787
http://cpb.iphy.ac.cn; http://iopscience.iop.org/cpb

What follows is a list of articles you may be interested in

Photogalvanic effects in surface states of topological insulators under perpendicular magnetic fields

Haoyu Li(李浩宇), Kainan Chang(常凯楠), Wang-Kong Tse, and Jin Luo Cheng(程晋罗)
Chin. Phys. B, 2026, 35 (**5**): 054203. DOI: 10.1088/1674-1056/ae4c68

Generation of wavelength-tunable, bound-state and noise-like pulses in an all-polarization-maintaining laser ring cavity based on nonlinear polarization evolution

Yazhou Shi(石亚洲), Ze Li(李泽), and Zhiguo Lv(吕志国)
Chin. Phys. B, 2026, 35 (**5**): 054202. DOI: 10.1088/1674-1056/ae15f3

Bistable Goos-Hänchen shift owing to leaky-mode excitation in a slab waveguide with Kerr nonlinear medium

Yuan-Ping Cai(蔡园平), Li Jiang(姜丽), and Ren-Gang Wan(万仁刚)
Chin. Phys. B, 2026, 35 (**4**): 044203. DOI: 10.1088/1674-1056/ae00b3

Tea polyphenol polymer film enables broadband optical modulation for hybrid mode-locked ultrafast fiber lasers

Wei Chen(陈伟), Kang Li(李康), Cheng Gao(高成), Qingping Hu(胡庆平), Zhengfan Li(黎征帆), Yi Xiong(熊祎), and Yunzhou Sun(孙运周)
Chin. Phys. B, 2026, 35 (**2**): 024209. DOI: 10.1088/1674-1056/ae156e

Theoretical and computational feasibility of femtosecond laser multifilament transverse structures reconstruction via circular-scanning-based photoacoustic tomography

Qingwei Zeng(曾庆伟), Lei Liu(刘磊), Shuai Hu(胡帅), and Shulei Li(李书磊)
Chin. Phys. B, 2025, 34 (**9**): 094209. DOI: 10.1088/1674-1056/ade663

INVITED REVIEW

Phonons at functional oxide interfaces: An *in situ* sum-frequency spectroscopic perspective

Shiyu Zhang(张诗雨), Junjie Dong(董俊杰), Tongying Liu(刘彤影), and Wei-Tao Liu(刘韡韬)†

Physics Department, State Key Laboratory of Surface Physics, Key Laboratory of Micro and Nano Photonic Structures of Ministry of Education (MOE), Fudan University, Shanghai 200433, *China*

(Received 10 February 2026; revised manuscript received 18 March 2026; accepted manuscript online 26 March 2026)

Functional oxides host emergent interfacial phenomena from superconductivity to catalysis, intimately tied to lattice phonons that mediate many-body interactions. Sum-frequency generation (SFG) spectroscopy, a second-order nonlinear optical technique with intrinsic surface specificity, enables *in situ* and *operando* probing of lattice vibrations at surfaces and interfaces. In this review, we introduce the basic theory of SFG and survey its application in investigating functional oxide surfaces and interfaces — tracking oxygen vacancies on anatase TiO_2, unveiling electron–phonon coupling modulation in $LaAlO_3/SrTiO_3$ heterostructures, and detecting polaronic signatures in Nb-doped $SrTiO_3$ — thereby offering microscopic insights into the physics of oxide interfaces.

Keywords: sum frequency spectroscopy, oxide interfaces, interfacial phonons, polarons

PACS: 42.65.–k, 68.35.Ja, 63.20.kd

DOI: 10.1088/1674-1056/ae5787 **CSTR:** 32038.14.CPB.ae5787

1. Introduction

In recent decades, functional oxide surfaces and interfaces have emerged as a forefront research focus in condensed matter physics and materials science. They exhibit a wealth of emergent phenomena not observed in their bulk counterparts, such as superconducting two-dimensional electron gas (2DEG),[1–4] Rashba spin–orbit coupling (SOC),[5–7] interface ferromagnetism,[8–10] and giant photoelectric response.[11,12] These phenomena primarily arise from the intricate interplay among charge, spin, orbital, and lattice degrees of freedom. For example, in 2010, the Caviglia group demonstrated continuous and reversible modulation of the Rashba coupling constant and spin splitting at the $LaAlO_3/SrTiO_3$ (LAO/STO) interface via an external gate voltage, confirming the critical influence of the interfacial electric field in tuning the Rashba effect.[5] In 2019, Hwang and co-workers first observed superconductivity in infinite-layer nickelate grown on an STO substrate, inferring a possible connection to orbital polarization.[13] In 2023, the Lee group reported persistent photoconductivity in LAO/STO, revealing that it originates from interactions between interfacial oxygen vacancies and electrons.[12]

Among the various factors determining the physical properties of functional oxides, phonons — the representative of lattice dynamics — play a crucial role. Phonons are quantized collective lattice vibrations (normal modes) that can be classified into acoustic or optical branches.[14] In functional oxides, metal–oxygen (M–O) stretching typically contributes to optical vibrational modes with sizeable dipole moments.[15] These modes are therefore closely related to the IR-active phonons frequently probed in vibrational spectroscopies.[16] At surfaces and interfaces, symmetry breaking, reconstruction, and defects can further localize or modify these M–O–related modes, giving rise to surface/interface phonons.[17,18] As quantized collective excitations of lattice vibrations,[14] phonons participate in a series of unique phenomena at surfaces and interfaces, such as localized interfacial electronic states,[19,20] band splitting,[21] and emergent modes,[22–24] due to lattice mismatch and interface reconstruction. Therefore, in-depth study of interfacial phonons is essential for understanding the corresponding microscopic mechanism. There have been extensive studies on lattice phonons in functional oxides. In 1994, Karmanenko and co-workers employed Raman spectroscopy to study $YBa_2Cu_3O_{7-\delta}/SrTiO_3/YBa_2Cu_3O_{7-\delta}$ heterostructures. Through analysis of the intensity of three Raman-active vibrational modes, the crystal orientations were determined, and the structural quality was assessed based on frequency shifts and the full width at half maximum (FWHM) of the Raman peaks.[25] In 2025, Xiong and co-workers combined electron energy loss spectroscopy (EELS) with ultrafast pump-probe spectroscopy to observe coherent optical phonons in FeSe/Nb:STO, revealing the strong electron–phonon coupling (EPC) of FeSe films and Nb:STO substrate, and providing evidence for its role in enhanced superconductivity.[26]

These systems involve buried interfaces, which necessi-

†Corresponding author. E-mail: wtliu@fudan.edu.cn

© 2026 Chinese Physical Society and IOP Publishing Ltd. All rights, including for text and data mining, AI training, and similar technologies, are reserved.

tate probing with penetrating capability. However, the increased penetration depth often compromises interfacial specificity. Sum-frequency generation (SFG) and second-harmonic generation (SHG) are techniques based on second-order nonlinear optical processes. Under the electric dipole approximation, only phonons at surfaces and interfaces exhibit the SFG response; therefore, it is capable of detecting signals from within a few monolayers at surfaces and interfaces.[27] Previously, SHG has been widely employed in studies of oxide interfaces.[28] It detects overall symmetry changes in interfacial electronic states, with its signal arising from non-resonant electronic nonlinear responses. Meanwhile, as a spectroscopic technique, SFG can further identify resonance modes by combining tunable infrared (IR) and fixed-frequency near-infrared (NIR) photons. This feature enables SFG to elucidate more underlying microscopic mechanisms associated with symmetry breaking, making it a powerful *in situ* experimental tool for exploring microscopic interfacial phonon behaviors.[27]

2. Theoretical basis

Sum-frequency generation arises from the second-order nonlinear polarization in a medium induced by optical fields.[29,30] The optical fields $\boldsymbol{E}(\omega_1)$ and $\boldsymbol{E}(\omega_2)$ interact and generate a nonlinear polarization $\boldsymbol{P}(\omega_3=\omega_1+\omega_2)$. Under the electric-dipole approximation, the SFG process is governed by the second-order nonlinear susceptibility tensor $\overleftrightarrow{\chi}^{(2)}$. This intrinsic material property determines the efficiency of three-wave mixing. Under the inversion symmetry operation, both the polarization $\boldsymbol{P}$ and the electric field $\boldsymbol{E}$ undergo a sign reversal. Consequently, the second-order nonlinear polarization, $\boldsymbol{P}^{(2)}=\varepsilon_0\overleftrightarrow{\chi}^{(2)}:\boldsymbol{E}(\omega_1)\boldsymbol{E}(\omega_2)$, remains self-consistent after the operation only if $\overleftrightarrow{\chi}^{(2)}=0$ in inversion symmetry systems. Nevertheless, the intrinsic symmetry breaking at surfaces and interfaces leads to the non-vanishing nonlinear susceptibility, $\overleftrightarrow{\chi}^{(2)}_{\mathrm{S}}\neq 0$, permitting the generation of the sum-frequency signal. It is this fundamental mechanism that endows SFG with its inherently high sensitivity to interfaces.[27]

For phonon spectroscopy, the SFG process consists of an IR and a Raman process. The corresponding quantum process is illustrated in the inset of Fig. 1. When a narrowband NIR beam and a tunable broadband IR beam overlap on the sample surface spatially and temporally, a coherent sum-frequency (SF) beam is generated. As the tunable infrared light frequency ω_{IR} coincides with an interfacial optical phonon mode ω_q, $\chi^{\leftrightarrow(2)}$ exhibits resonant enhancement, giving rise to a characteristic peak in the sum-frequency spectrum. This process is described by

$$\overleftrightarrow{\chi}^{(2)}=\overleftrightarrow{\chi}^{(2)}_{\mathrm{NR}}+\sum_q\frac{\overleftrightarrow{A}^{(2)}_q}{\omega_{\mathrm{IR}}-\omega_q+\mathrm{i}\Gamma_q}.$$

Here, $\overleftrightarrow{\chi}^{(2)}_{\mathrm{NR}}$ is the nonresonant contribution, while $\overleftrightarrow{A}^{(2)}_q$, ω_q, and Γ_q denote the amplitude, resonant frequency, and the damping coefficient of the q^{th} resonance.[29] Thus $\overleftrightarrow{\chi}^{(2)}$ embodies the quantum mechanical probability for the optical transition. Under the quantum mechanical framework, $\overleftrightarrow{A}^{(2)}_q$ is proportional to the product of the Raman polarizability and the IR dipole derivative for the q^{th} mode:

$$\overleftrightarrow{A}^{(2)}_q\propto\frac{\partial\overleftrightarrow{\alpha}^{(1)}}{\partial Q_q}\frac{\partial\mu}{\partial Q_q}.$$

Here, the Raman polarizability $\frac{\partial\overleftrightarrow{\alpha}^{(1)}}{\partial Q_q}$ and the IR dipole derivative $\frac{\partial\mu}{\partial Q_q}$ respectively determine Raman and IR activities of the q^{th} mode. This relationship delineates another fundamental selection rule in the SFG process: only vibrational modes exhibiting both infrared and Raman activity are detectable in the SFG phonon spectrum.[31]

The SFG interaction complies with the conservation of energy and in-plane momentum:

$$\begin{aligned}&\hbar\omega_{\mathrm{SF}}=\hbar\omega_{\mathrm{NIR}}+\hbar\omega_{\mathrm{IR}},\\&k_{\parallel}(\omega_{\mathrm{SF}})=k_{\parallel}(\omega_{\mathrm{NIR}})+k_{\parallel}(\omega_{\mathrm{IR}}),\end{aligned}$$

$\Delta k=|k_{\perp}(\omega_{\mathrm{SF}})-k_{\perp}(\omega_{\mathrm{NIR}})-k_{\perp}(\omega_{\mathrm{IR}})|$ is the wave vector mismatch in the interface vertical direction, and $l_{\mathrm{c}}=1/\Delta k$ is the optical coherence length of the SFG process. For certain oxides, there may exist a strong surface electric field, which can effectively break the inversion symmetry within the space charge region. This leads to an effective bulk nonlinear optical contribution $\overleftrightarrow{\chi}^{(2)}_{\mathrm{B}}$, and the total $\overleftrightarrow{\chi}^{(2)}$ is expressed as $\overleftrightarrow{\chi}^{(2)}=\overleftrightarrow{\chi}^{(2)}_{\mathrm{S}}+\mathrm{i}\overleftrightarrow{\chi}^{(2)}_{\mathrm{B}}l_{\mathrm{s}}$. Here l_{s} is the smaller of l_{c} and l_{f}, where l_{f} is the thickness of the surface field across the space charge region.[32]

The intensity of this SFG signal is given by

$$\begin{aligned}I(\omega_{\mathrm{SF}})&\propto\left|\chi^{(2)}_{\mathrm{eff}}\right|^2\\&=\left|[\hat{e}_{\mathrm{SF}}\cdot\overleftrightarrow{L}_{\mathrm{SF}}]\cdot\overleftrightarrow{\chi}^{(2)}:[\overleftrightarrow{L}_{\mathrm{NIR}}\cdot\hat{e}_{\mathrm{NIR}}][\overleftrightarrow{L}_{\mathrm{IR}}\cdot\hat{e}_{\mathrm{IR}}]\right|^2.\end{aligned}$$

Here, $\chi^{(2)}_{\mathrm{eff}}$ is the effective second-order nonlinear susceptibility. ω_i, $\overleftrightarrow{L}_i$, and $\hat{e}_i$ denote the angular frequency, the tensorial Fresnel transmission coefficient, and the unit polarization vector, respectively, with the subscript i representing the SF, NIR, and IR beams. By measuring spectra with different beam polarization combinations (e.g., SSP denotes S-polarized SF output, S-polarized NIR input, and P-polarized IR input, respectively), the tensor elements of $\chi^{(2)}_{\mathrm{eff}}$ can be deduced. For instance,

$$\chi^{(2)}_{\mathrm{SSP}} = [0, L_{yy}(\omega_{\mathrm{SF}}), 0]\overset{\leftrightarrow}{\chi}^{(2)} : \begin{bmatrix} 0 \\ L_{yy}(\omega_{\mathrm{NIR}}) \\ 0 \end{bmatrix} \begin{bmatrix} L_{xx}(\omega_{\mathrm{IR}})\cos\theta_{\mathrm{IR}} \\ 0 \\ L_{zz}(\omega_{\mathrm{IR}})\sin\theta_{\mathrm{IR}} \end{bmatrix},$$

$$\chi^{(2)}_{\mathrm{PPP}} = [-L_{xx}(\omega_{\mathrm{SF}})\cos\theta_{\mathrm{SF}}, 0, L_{zz}(\omega_{\mathrm{SF}})\sin\theta_{\mathrm{SF}}]\overset{\leftrightarrow}{\chi}^{(2)} : \begin{bmatrix} L_{xx}(\omega_{\mathrm{NIR}})\cos\theta_{\mathrm{NIR}} \\ 0 \\ L_{zz}(\omega_{\mathrm{NIR}})\sin\theta_{\mathrm{NIR}} \end{bmatrix} \begin{bmatrix} L_{xx}(\omega_{\mathrm{IR}})\cos\theta_{\mathrm{IR}} \\ 0 \\ L_{zz}(\omega_{\mathrm{IR}})\sin\theta_{\mathrm{IR}} \end{bmatrix}.$$

Here, (x, y, z) are the laboratory coordinates, with x–z taken as the plane of incidence, where θ_i represents the angle between the i^{th} beam and the normal. The $\overset{\leftrightarrow}{\chi}^{(2)}$ elements expressed in the laboratory coordinates (x, y, z) are related to those in the crystal coordinates (a, b, c) by

$$\chi^{(2)}_{ijk} = \sum_{lmn} \chi^{(2)}_{lmn} (\hat{\boldsymbol{i}}\cdot\hat{\boldsymbol{l}})(\hat{\boldsymbol{j}}\cdot\hat{\boldsymbol{m}})(\hat{\boldsymbol{k}}\cdot\hat{\boldsymbol{n}}),$$

where $i, j, k \in \{x, y, z\}$, $l, m, n \in \{a, b, c\}$. In our SFG measurements, as shown in Fig. 1, (x, y, z) are established with the z-axis oriented along the sample surface normal (as well as the c-axis), and the a-axis perpendicular to the incident plane [translucent vertical plane in Fig. 1]. When the crystal φ-axis is oriented at an angle φ relative to the plane of incidence, the unit vectors in the crystal frame transform into the laboratory frame as $\hat{a} = \cos\varphi\hat{x} + \sin\varphi\hat{y}$, $\hat{b} = -\sin\varphi\hat{x} + \cos\varphi\hat{y}$, and $\hat{c} = \hat{z}$.

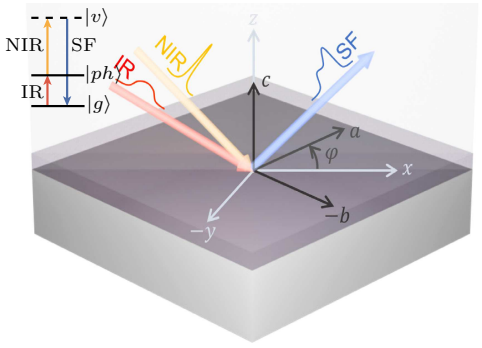


Fig. 1. The experimental configuration with the sample placed at an azimuthal angle φ with respect to the beam incident plane. The yellow, red, and blue beams denote NIR, IR, and SF beams, respectively. Inset: The transition diagram of an SFG process for phonon detection. An IR photon excites a phonon coherence ($|ph\rangle$) from the ground state ($|g\rangle$), upconverted by a NIR photon to a virtual state ($|v\rangle$, an intermediate state derived from nearby electronic states), and emits an SF photon.

The structural symmetry of a medium governs the symmetry of its nonlinear susceptibility tensors. More specifically, each crystal point group defines a distinct set of symmetry operations, dictating which tensor elements vanish and which are interrelated. Therefore, through the analysis of tensor elements, microscopic information at the interface, such as structural symmetry, can be derived, as we shall elaborate below.

3. SFG phonon spectroscopy of selected oxides

3.1. Anatase TiO_2 surface

We adopted the widely studied (101) surface of anatase TiO_2 as a demonstration to illustrate how SFG can be employed to probe surface phonons and characterize their physical properties.[22] Raman spectroscopy (blue curve) in Fig. 2(a) showed the two highest-frequency Raman-active transverse optical (TO) phonon modes of the bulk anatase at 543 cm^{-1} and 667 cm^{-1}.[22,33] However, the SFG spectrum of the same sample (red curve) revealed a new resonance peak at $\sim$ 860 cm^{-1}. By combining with first-principles calculations, we assigned this vibrational mode to the stretching vibration between the five-coordinated surface titanium ions [Ti(5c)] and their adjacent three-coordinated oxygen ions [O(3c)], as shown in Fig. 2(b). Ti(5c) is a highly localized active site on the anatase (101) surface, and this phonon mode serves as a direct "spectral fingerprint" for characterizing such surface active sites.

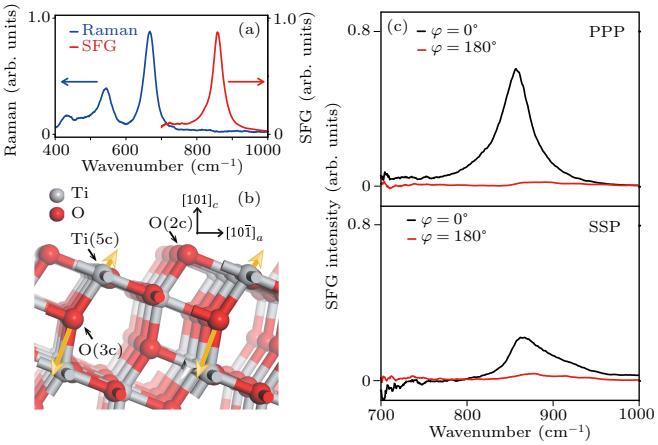


Fig. 2. Structure and phonon spectra of the anatase(101) surface. (a) Reflected Raman (blue curve) and SFG (red curve) spectra from an anatase(101) surface, with all beams being P-polarized. (b) Structure of anatase(101). Ti(5c), O(2c), and O(3c) denote five-coordinated surface titanium, two and three-coordinated oxygen ions, respectively. Yellow arrows describe the displacements of Ti(5c) and O(3c) associated with the surface phonon mode. (c) SFG spectra at various φ with different beam polarization combinations. Black (red) curves are spectra taken at $\varphi = 0°$ (180°). Data adapted from Ref. [22].

We applied symmetry analysis to interpret the spectral features. The anatase(101) surface belongs to the C_{1v} point group and exhibits mirror symmetry with respect to the plane perpendicular to the [010] axis. We set $a \parallel [10\bar{1}]$ (parallel to the mirror plane), $b \parallel [010]$ (perpendicular to the mirror plane), and $c \parallel [101]$ (corresponding to the surface normal). The C_{1v} point group contains the symmetrical operations: $a \to a$, $b \to -b$, $c \to c$.[34] Based on the relationship between the vibrations and this mirror plane, they are classified into two irreducible representations: A' and A''. The A' mode is symmetric with respect to the mirror plane, and the infrared transition dipole moment lies parallel to the plane. The

A'' mode is antisymmetric with respect to the mirror plane, with the infrared transition dipole moment perpendicular to it. First-principles calculations indicated that the 860 cm^{-1} mode belongs to the A' irreducible representation. Based on point-group symmetry analysis, the response of the anisotropic A' mode corresponding to $\phi = 0°$ (Fig. 1) and 180° in the SSP and PPP spectra is described as

$$\chi^{(2)}_{\parallel}(\mathrm{SSP})|_{A'} = [\pm\mu_a \cdot \cos\theta_{\mathrm{IR}} L^{\parallel}_{xx}(\omega_{\mathrm{IR}}) + \mu_c \cdot \sin\theta_{\mathrm{IR}} L^{\parallel}_{zz}(\omega_{\mathrm{IR}})],$$
$$\chi^{(2)}_{\parallel}(\mathrm{PPP})|_{A'} = [\pm\mu_a \cdot \cos\theta_{\mathrm{IR}} L^{\parallel}_{xx}(\omega_{\mathrm{IR}}) + \mu_c \cdot \sin\theta_{\mathrm{IR}} L^{\parallel}_{zz}(\omega_{\mathrm{IR}})].$$

Here μ_a (μ_c) is the infrared transition dipole moment along the a (c) axis. The sign "+" ("−") corresponds to $\phi = 0°$ (180°). Figure 2(c) shows the azimuth-dependent spectral response under different polarization combinations, in line with the A' irreducible representation. Furthermore, the spatial orientation of Ti(5c)–O(3c) bonds can be deduced from quantitative tensor element analysis based on the spectral anisotropy. We obtained $|(\mu_a/\mu_c)| \approx 0.47 \pm 0.02$, which represents the projection of transition dipole moments. Based on the above, the dipole moment tilting angle from the c-axis ([101]) was derived as $\arctan(\mu_a/\mu_c) \approx 25 \pm 5°$, close to the theoretical prediction. This finding confirms the assignment of the 860 cm^{-1} mode and verifies the surface-specific origin of SFG spectra.

We used the identified ~ 860 cm^{-1} surface phonon mode as an *in situ* probe to track the structural evolution of the anatase(101) surface under *operando* ultraviolet (UV) irradiation. The UV light has a central wavelength of 368 nm and a power density of about 20 mW/cm^2. Under ambient conditions, the SFG signal intensity of the ~ 860 cm^{-1} surface phonon mode decreased sharply upon UV illumination in Fig. 3(a). This is attributed to the formation of surface oxygen vacancies [V_O^{surf}, shown in Fig. 3(b)].[35] UV radiation reduces the stability of oxygen vacancies, activating their migration from the bulk to the surface. On the anatase(101) surface, oxygen vacancies preferentially form at two-coordinated oxygen sites, causing the adjacent Ti(5c) to transform into a four-coordinated [Ti(4c)] configuration.[36,37] Since the SFG signal intensity is proportional to the areal density of surface Ti(5c) sites, the reduction in Ti(5c) concentration directly leads to the observed signal attenuation. Consequently, the decrease in SFG signal intensity reflects an increase in the population of V_O^{surf}.

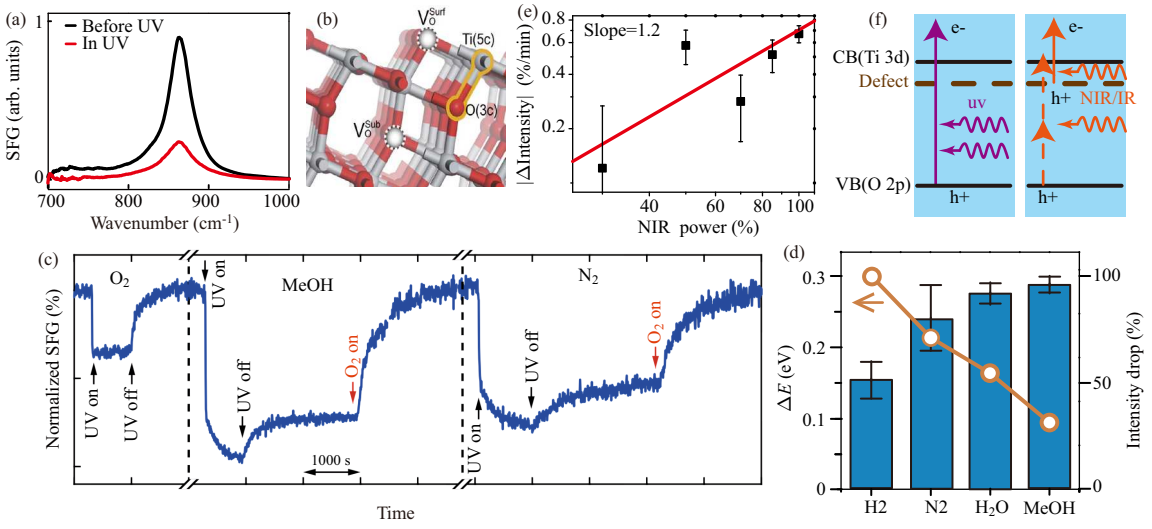


Fig. 3. *Operando* SFG phonon spectra from anatase(101) under various conditions. (a) Spectra in pure nitrogen gas before (grey curve) and in (red curve) UV irradiation, with PPP polarization combination. (b) Preferential locations of V_O^{surf} and V_O^{sub} on anatase(101), marked with dashed circles. (c) Evolution of the phonon intensity in pure oxygen, saturated methanol vapor, and pure nitrogen gases in response to UV irradiation and oxygen dosage. (d) Energy difference $\Delta E = E(V_O^{surf}) - E(V_O^{sub})$ in various ambient gases obtained from *ab initio* calculation (open circles). Vertical columns represent percentage drop of the 860 cm^{-1} peak after a constant UV irradiance in various ambient gases. (e) Power dependence of the surface phonon intensity drop with respect to the NIR irradiation power. Straight line is a polynomial fit. (f) Excitation schematics upon the UV (left panel) or NIR (right panel) irradiations. Data adapted from Refs. [22,41].

To confirm that the variation of the SFG signal was derived from V_O^{surf}, we conducted measurements in different gas environments. In a pure oxygen environment, the 860 cm^{-1} signal decreased only slightly upon UV irradiation and fully recovered after the UV was switched off. This indicates that V_O^{surf} were replenished by oxygen. In other ambient gases, the intensity reduction under UV exposure was more pronounced than in oxygen, as shown in Fig. 3(c). Notably, although the 860 cm^{-1} peak diminished under UV irradiation, it did not vanish completely. This indicates that while UV exposure promotes the generation of V_O^{surf}, these vacancies are inherently unstable and tend to migrate inward, forming subsurface vacancies [V_O^{sub}, shown in Fig. 3(b)]. These two competing processes reach a dynamic balance, resulting in a finite concentration of V_O^{surf}. Experimentally, in methanol vapor, water vapor, nitrogen, and hydrogen, the percentage drop of SFG intensity

after UV exhibited an inverse correlation with the calculated energy difference (ΔE) between V_O^{surf} and V_O^{sub} in Fig. 3(d). This observation confirmed that the stability of V_O^{surf} varies with ambient conditions. Here, methanol and water slightly dope the surface conduction band with their oxygen lone pair electrons, thereby enhancing the stability of V_O^{surf}.[38–40] Nitrogen and hydrogen produce a low surface coverage through van der Waals interaction with the anatase surface, contributing to a certain stabilizing effect on oxygen vacancies.[22]

Notably, we observed a gradual drop in the surface phonon intensity of the anatase(101) surface upon continuous irradiation with NIR and IR photons.[41] This shows that even low-energy photons can increase the V_O^{surf} densities at the anatase surface. Figure 3(e) shows the percentage of photon intensity drop per unit time with the NIR power varied (relative to the full power). On the double-logarithmic scale, the signal drop rate shows a power-law slope of about 1.2. This suggests that the two-photon contribution is minor in our case [orange dashed line in the right panel of Fig. 3(f)]. However, since the bandgap of anatase is about 3.2 eV, the 1.5 eV NIR photons cannot directly excite electrons from the O-2p band via one-photon absorption. Thereby, the NIR photons dope the sample with electrons via defect band absorption [orange solid line shown in the right panel of Fig. 3(f)] and increase the relative stability of surface oxygen vacancies.

To conclude, through the measurements of anatase(101), we demonstrate the high specificity of SFG spectroscopy in probing surface phonons and elaborate on the phonon vibrational features by symmetry analysis. Beyond its sensitivity to lattice vibrations, SFG is also responsive to localized surface defects. These two factors jointly govern the observed phonon behaviors.

3.2. LAO/STO heterointerface

SFG can also be utilized to study heterostructures with many-body interactions such as EPC. $LaAlO_3/SrTiO_3$ (LAO/STO) is a classical heterointerface with a series of fascinating properties, including the formation of an interfacial 2DEG[1] with superconductivity,[2] tunable magnetic ordering by defects,[8] and many more. Phonons play a prominent role among these various phenomena, which motivated us to probe the phonon modes at this LAO/STO interface by SFG.[32]

In bulk-STO, there is no SFG response because of its centrosymmetric feature. At the surface, the truncation lowers the symmetry from the bulk O_h point group (at room temperature) to the non-centrosymmetric C_{4v} group. Lifting the degeneracies of the phonon modes and Ti-3d states removes the pure parity of the resulting energy levels. This enables SFG transitions that are symmetry-forbidden in the bulk. At the STO(001) bare substrate surface, a pronounced SFG resonance was observed around 103 meV [in Fig. 4(a)], which is attributed to the coupling of Ti-3d electrons and a surface phonon mode. This mode is the highest zone-center longitudinal optical (LO_4) phonon mode in bulk-STO, corresponding to Ti–O out-of-phase stretching vibration in TiO_6 octahedra. Other techniques such as high-resolution electron energy loss (HR-EELS) can also detect Fuchs–Kliewer (FK) type of phonons. Figure 4(b) presents EELS results of the bare STO substrate (red curve) reported by the Feng group,[42] showing two distinct loss peaks at ~ 60 meV (corresponding to the LO_3 mode) and ~ 92 meV (corresponding to the LO_4 mode), determined by the pole in $\mathrm{Im}[1/(\tilde{\varepsilon}(\omega)+1)]$ [light brown curve in Fig. 4(c), with $\tilde{\varepsilon}$ being the complex optical dielectric constant of bulk-STO] due to the FK mechanism.[43] In optical spectra, the LO_4 mode peaks at ~ 101 meV, determined by the pole in $\mathrm{Im}[\tilde{\varepsilon}^{-1}(\omega)]$ (deep brown curve).[44] The phonons detected by EELS respond in different frequencies compared to those observed by SFG, which is due to the broken symmetry at the surface and greater localization. Relative to the bulk LO_4 mode near 101 meV, the blueshift of the surface mode in SFG spectra is ascribed to the slight shortening of the Ti–O bonds at the truncated surface. We further tested the surface specificity of SFG by comparing the TiO_2-terminated surface with the mixed (TiO_2 and SrO)-terminated surface, and the latter exhibited a weaker SFG response [red curve in Fig. 4(a)] owing to the presence of non-truncated octahedra, verifying that the 103 meV resonance observed in SFG spectra is highly localized. The nonlinear optical susceptibility strength [$\chi^{(2)}$] of the 103 meV phonon on bare STO(001) was estimated to be 5×10^{-20} m^2/V, which is about an order of magnitude stronger than the typical value of a molecular monolayer.[30]

We then deposited different thicknesses of LAO overlayers on STO and conducted SFG measurements. As the single-crystalline LAO overlayer thickness increased from 1 to 6 unit cells (uc) on STO, the surface-phonon spectra changed markedly. These changes strongly correlate with the insulator-to-metal transition [Figs. 4(d) and 4(e)]. With LAO coverages of 1 uc and 2 uc, the SFG signal intensity dropped significantly. Since the lattice modes of LAO lie far outside this frequency range,[45] the signal variation must come from the same LO_4-derived vibration observed in the STO substrate. It indicates the partial restoration of inversion symmetry at the interface due to lattice strain.[46] Correspondingly, the phonon peaks showed a slight redshift of ~ 1 meV from that of the bare STO(001) substrate. At the subcritical thickness of 3 uc LAO (just below the threshold for 2DEG formation), the SFG intensity increased abruptly. Although the LAO overlayer restores the interfacial Ti–O bond lengths close to those in the bulk STO,[47,48] previous SHG studies on the same system had revealed an extra electric field-induced (EFI) contribution in 3 uc LAO/STO.[49] In this situation, the ferroelectric (FE) distortion within the LAO layer establishes a dipolar field pointing

away from STO [shown in Fig. 4(f)],[50,51] which induces substantial orbital reconstruction and electronic structure asymmetry at the interface, thereby strongly enhancing the SFG response. With 2DEG forming at 4 uc and beyond, the persistent EFI effect was evidenced by the strong SHG signal reported by Marrucci and co-workers.[49] However, a sharp decrease in the SFG intensity was simultaneously observed. It is assumed to be due to dynamic screening by the conducting carriers in the 2DEG,[52] which suppresses the long-range electron–phonon interaction. This screening mechanism is supported by experimental evidence: the spectra of the insulating samples with post-growth annealing in oxygen were restored like that of 3 uc, compared with the suppressed SFG signal of the high carrier concentration samples, shown in Figs. 4(g) and 4(h). The estimated Thomas–Fermi screening length is $r_{\mathrm{TF}} = \sqrt{\varepsilon\varepsilon_0 E_{\mathrm{F}}/(2e^2 n_{3\mathrm{D}})}$.[53] It is comparable to the polaron radius $r_{\mathrm{p}} = \sqrt{\hbar/(2m^*\Omega_{\mathrm{LO4}})} \approx 0.6$ nm[52] of the $\mathrm{LO_4}$ mode, further validating the presence of Coulomb screening by the 2DEG to EPC at the LAO/STO interface.

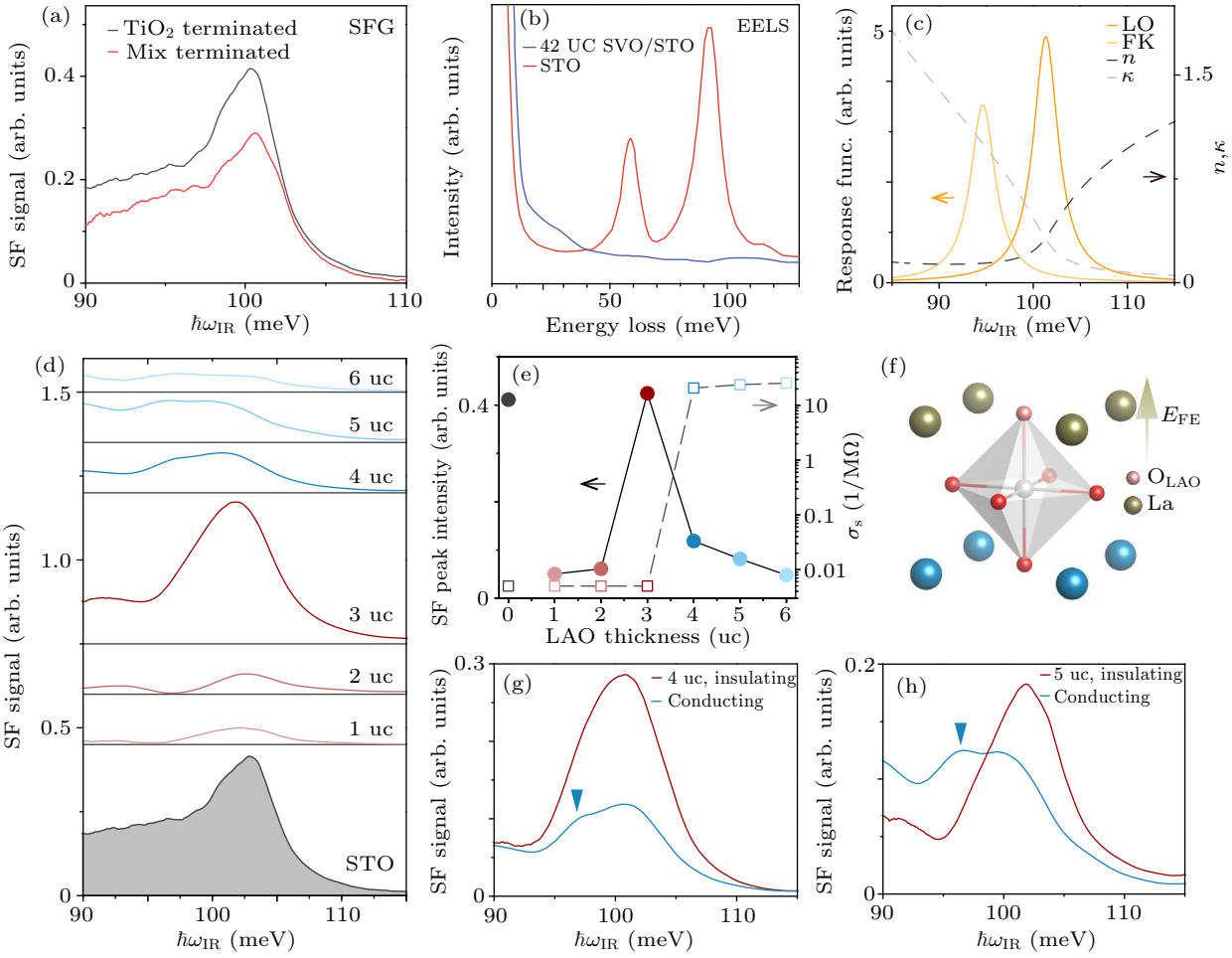


Fig. 4. SFG phonon spectroscopy study of the LAO/STO heterostructure. (a) Spectra from STO(001) surfaces with different terminations: $\mathrm{TiO_2}$ terminated surface (black curve) and untreated surface with mixed terminations (red curve). (b) EELS spectra of bare (red curve) and SVO-covered STO substrates. Data adapted from Ref. [42]. (c) Real and imaginary parts of STO bulk refractive indices (dashed lines); calculated response functions of the $\mathrm{LO_4}$ phonon and the corresponding FK mode (brown curves). (d) SFG spectra from the $\mathrm{TiO_2}$-terminated STO(001) surface (bottom panel, black curve filled in gray) and those covered by 1 to 6 uc of LAO epitaxial layers (colored curves). The spectra are offset for clarity with corresponding baselines marked in gray. (e) SFG phonon peak intensity (solid circles) and sheet conductance (open squares) versus the LAO layer thickness. The color scheme of data points is the same as that in (d). (f) $\mathrm{TiO_6}$ octahedron at the LAO/STO interface. The arrow represents the built-in dipolar field due to FE distortion in LAO layer $\lesssim 3$ uc. (g) and (h) SFG spectra from 4 uc and 5 uc samples: annealed in oxygen (red curves) and conducting (blue curves) for comparison. Data adapted from Ref. [32].

In addition to the 103 meV mode, another resonant feature near 96–98 meV had also been identified by SFG [Figs. 4(g) and 4(h), marked by triangles]. For insulating 4 uc and 5 uc samples annealed in oxygen, this low-frequency mode became barely discernible, suggesting its origin from the oxygen vacancies [$\mathrm{V_O}$, shown in Fig. 5(a)]. This point is supported by the phonon dispersion calculations by the Gong group in 2015, which exhibited that $\mathrm{V_O}$ would induce a surface polar mode at the Γ point near 93.6 meV in STO(001) [Fig. 5(b)].[54] For further verification, we measured SFG spectra of insulating STO after 365 nm (3.40 eV) UV irradiation, observing the enhanced low-frequency mode [purple curve in Fig. 5(c)]. This mode is more pronounced in spectra with the PPP (P-polarized SF, P-polarized NIR, and P-

polarized IR) polarization combination than in the SSP (S-polarized SF, S-polarized NIR, and P-polarized IR). Here, SSP primarily probes out-of-plane dipole moments at the fourfold-symmetric STO(001) surface, whereas PPP is sensitive to both out-of-plane and in-plane moments.[22] This indicates that the associated vibration carries greater in-plane dipole moment components, consistent with the characteristic of the V_O-related Ti–O stretching motion which has a large in-plane component due to the lattice distortion around V_O.

Therefore, SFG provides a direct approach for *in situ* detection of oxygen vacancies at interfaces. To improve the quality of the 2DEG devices, the Cheng group designed $(m+n)$ uc LAO/STO interfaces (m uc interfacial buffer LAO layers with the major defects deliberately suppressed, and n uc top LAO layers generating V_O donors).[55] Our SFG spectra [Fig. 5(d)] show that the V_O-related mode at 96 meV was significantly suppressed in modulation-doped $(3+2)$ LAO/STO compared to the conventional $(5+0)$ uc structure where it remained prominent.[32] The $(3+2)$ sample, featuring fewer interfacial V_O, exhibits high transport mobility [Fig. 5(e), sample A], along with a low-field quantum oscillation showing anomalous characteristics. The SFG measurements provide compelling evidence that the stepwise growth technique minimizes interfacial V_O defects, thereby enabling the fabrication of higher-quality devices.[56] Crucially, these results demonstrate that interfacial V_O is not a prerequisite for the formation of the 2DEG.

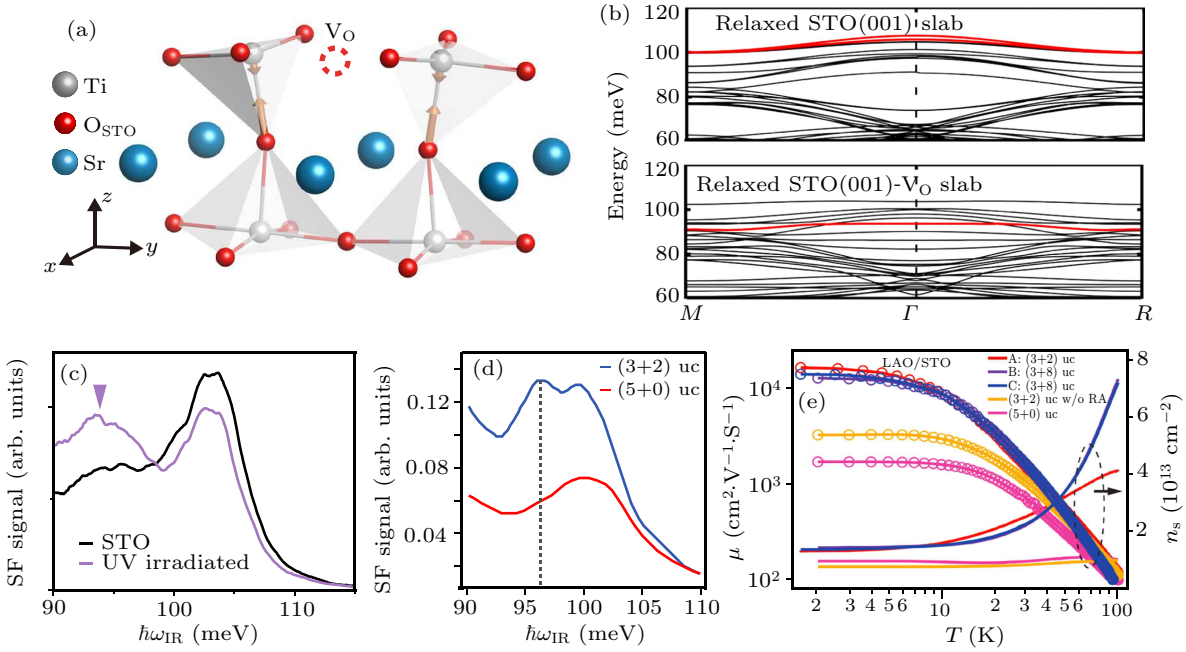


Fig. 5. The V_O related SFG response on STO(001). (a) Normal mode coordinates of the local vibration around V_O (dotted red circle) in STO, with displacements of Ti and O ions marked by orange arrows. The neighboring TiO_6 octahedra are distorted due to the change in bonding strength. (b) Calculated phonon dispersion. The upper and lower panels show the relaxed STO (001) slab and the relaxed STO(001)-V_O slab, respectively. Data adapted from Ref. [54]. (c) SFG spectra from a TiO_2-terminated STO(001) substrate before (black curve) and after (purple curve) 30 min of UV irradiation in vacuum. Arrow indicates an enhanced mode at 94 meV. (d) SFG spectra of a $(5+0)$ sample (blue curve) and a $(3+2)$ sample (red curve), suggesting the suppression of V_Os at the interface of the $(3+2)$ sample. (e) Temperature dependence of carrier density and low-field ($B = 0.5$ T) mobility (weighted average of all subbands). The modulation-doped samples (A, B, and C) show the highest mobilities. Data adapted from Ref. [55].

3.3. Nb:STO and monolayer FeSe/Nb:STO heterostructure

Over the past decade, enhanced interfacial superconductivity has been discovered in few-unit-cell FeSe films grown on Nb-doped $SrTiO_3$ (Nb:STO), exhibiting a critical temperature (T_c) significantly higher than that of bulk FeSe and FeSe films grown on undoped STO.[26,57] This motivated us to employ SFG spectroscopy to investigate the interfacial phonons in this system. As shown in Fig. 6(a), compared with undoped STO(001) (pink curve), Nb:STO(001) (blue curve) exhibits a sharp resonance close to 99 meV, which is notably redshifted in frequency and significantly enhanced in intensity. After epitaxially growing a 1 uc FeSe layer on Nb:STO, the phonon signal drops substantially (purple curve). It remains stronger than that of undoped STO, and the resonance peak stays at its redshifted position.

For the above phenomena, we provide a brief discussion of the underlying mechanisms. In Nb:STO, Nb^{5+} doping in STO draws electron density around O^{2-} away from Ti^{4+}, thereby weakening the electrostatic attraction between Ti^{4+} and O^{2-}, as supported by the Bader charge analysis reported by Shen and co-workers.[58] Additionally, first-principles calculations of the TiO_2-terminated Nb:STO(001) surface reported by Franchini and co-workers revealed that Nb dop-

ing promotes the formation of localized small polarons at the STO(001) surface,[59] which elongates the Ti–O bonds.[60] The above analyses indicate that Nb doping leads to a reduction in the strength of the Ti–O bonds in STO, which directly lowers the phonon frequency, explaining the observed redshift of ~ 4 meV from undoped STO. Moreover, Nb doping in STO induces a strong surface field in the space charge region,[21,61] which enhances the effective field-induced second-order nonlinear optical susceptibility and results in the significant SFG intensity.[27] The decrease in the signal for FeSe/Nb:STO is attributed to dynamic screening by conducting carriers within the FeSe layer,[57] consequently reversing the enhancement effect of Nb doping on the nonlinear optical response and causing the SFG signal to fall back.

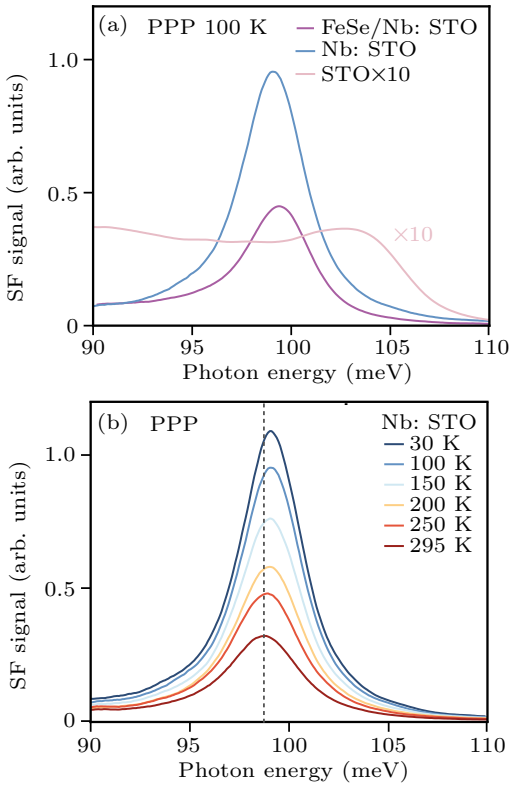


Fig. 6. LO_4-derived SF phonon spectra at STO and 0.5 wt% Nb:STO surfaces, and 1 uc FeSe/Nb:STO interface. (a) PPP spectra measured at 100 K; the STO signal is multiplied by ten times for clarity. (b) Temperature-dependent PPP spectra of Nb:STO. Dashed line indicates the peak position at 295 K (98.7 meV) to guide eyes.

Figure 6(b) shows the temperature dependence of the spectral response at the Nb:STO surface. During cooling, the resonance frequency exhibits a slight blueshift while the signal intensity gradually increases. As the temperature decreases from 295 K to 100 K, the unit cells of STO contract overall, leading to shortened Ti–O bonds (estimated $\Delta d_{\mathrm{Ti-O}} \approx 3.6 \times 10^{-3}$ Å).[62] Therefore, the phonon mode slightly hardens and its vibrational frequency exhibits a blueshift. Simultaneously, in Nb:STO, the exponential decrease in carrier concentration with cooling[63,64] widens the space charge region (W) to provide sufficient ionized donors for charge neutrality.[21,61] The relative permittivity is given by $\varepsilon_{\mathrm{r}} = \varepsilon_{\mathrm{l}} + C/(T - T_{\mathrm{C}})$, with ε_{l} the dielectric constant extrapolated to infinite temperature, T_{C} the Curie temperature, and C a constant.[65,66] While ε_{r} of Nb:STO increases at low temperatures, the growth of W^2 is overwhelmingly dominant. Consequently, the surface potential $\phi_{\mathrm{s}} \propto W^2/\varepsilon_{\mathrm{r}}$[61] exhibits a net increase as temperature drops, effectively strengthening the nonlinear optical response and leading to the notable enhancement in SFG signals.

Based on the analysis of the SFG spectra, Nb:STO exhibits distinct polaron behaviors and a stronger surface potential compared with undoped STO. These two features collectively delineate the physical picture that modifies the interfacial phonon behaviors and may contribute to the enhanced superconductivity observed in FeSe films grown on Nb:STO substrates.

4. Summary and outlook

To summarize, we provide an overview of SFG phonon spectroscopy in this review. We first introduce the fundamental principle of SFG, including the physical origin of its interfacial selectivity, the mechanism of signal generation, and its capability to resolve interfacial microstructure through different polarization combinations. Based on the above, we elaborate on its unique advantages and applications in studying interfacial phonon behaviors of functional oxides. SFG not only investigates the frequency, intensity, and symmetry of interfacial lattice vibrations, but also reveals their intrinsic correlations with interfacial electronic structures, defect states, and external field modulations, providing compelling experimental evidence for a mechanistic understanding of such functional oxide interfaces. As the field progresses, SFG phonon spectroscopy holds considerable promise for extending beyond the model systems described above. For example, the emergence of anisotropic superconductivity at $LaAlO_3/SrTiO_3$ interfaces represents a particularly compelling frontier,[3] where SFG phonon spectroscopy could provide new insights into the interplay between lattice anisotropy and unconventional pairing mechanisms. Technically, however, two challenges must be addressed. First, current IR laser frequencies are still too high to probe the soft phonon modes that are key to BCS superconductivity; second, laser-induced heating of sample surfaces demands better temperature control and enhanced detection sensitivity to permit measurements at lower laser powers. These underscore the need for continued technical advancement.

Moreover, there are two particularly valuable future directions. First, SFG spectroscopy can be applied to nanoparticle or colloidal systems. In their pioneering work, Dai, Roke, and coworkers have established the theoretical foundation and experimental protocols for SHG and SFG studies on colloidal particles.[67,68] The same methodology is applicable to SFG phonon spectroscopy and helps reveal the structures

of nanoparticle facets and how they interact with adsorbates. Technical challenges include strong optical attenuation and/or scattering, enhanced nonresonant backgrounds, and especially spectral congestion from multiple facets and other heterogeneous surface structures.[69] These could pose limitations on the detection sensitivity and frequency range, which require careful handling.

Another field of interest is the inclusion of ultrafast time-resolved capabilities in SFG phonon spectroscopy.[70,71] Using photocatalytic TiO_2 as an example, with multiple-color excitation and probing, we can monitor the evolution of surface phonons under the influence of photo-excited carriers as well as transient organic and/or aqueous adsorbates, which would provide rich information about their mutual interplay and new insight into photocatalytic reactions. Looking forward, we envision SFG phonon spectroscopy evolving into a versatile platform, serving as an indispensable tool for probing interfacial lattice dynamics and helping guide the rational design of functional oxides with optimized phonon-mediated properties.

Acknowledgements

We acknowledge support from the National Natural Science Foundation of China (Grant No. 12250002), the National Key Research and Development Program of China (Grant No. 2024YFA1409803), and the Science and Technology Commission of Shanghai Municipality (Grant Nos. 23JC1400400 and 23DZ2260100).

References

[1] Ohtomo A and Hwang H Y 2004 *Nature* **427** 423
[2] Reyren N, Thiel S, Caviglia A D, Kourkoutis L F, Hammerl G, Richter C, Schneider C W, Kopp T, Rüetschi A, Jaccard D, Gabay M, Muller D A, Triscone J and Mannhart J 2007 *Science* **317** 1196
[3] Chen Z, Liu Y, Zhang H, Liu Z, Tian H, Sun Y, Zhang M, Zhou Y, Sun J and Xie Y 2021 *Science* **372** 721
[4] Ren T S, Li M C, Sun X K, Ju L L, Liu Y, Hong S Y, Sun Y Q, Tao Q, Zhou Y, Xu Z and Xie Y W 2022 *Sci. Adv.* **8** eabn4273
[5] Caviglia A D, Gabay M, Gariglio S, Reyren N, Cancellieri C and Triscone J 2010 *Phys. Rev. Lett.* **104** 126803
[6] King P D C, He R H, Eknapakul T, Buaphet P, Mo S K, Kaneko Y, Harashima S, Hikita Y, Bahramy M S, Bell C, Hussain Z, Tokura Y, Shen Z X, Hwang H Y, Baumberger F and Meevasana W 2012 *Phys. Rev. Lett.* **108** 117602
[7] Xu H, Li H and Gauquelin N, *et al*. 2024 *Adv. Mater.* **36** 2313297
[8] Park D S, Rata A D and Maznichenko I V, *et al.* 2020 *Nat. Commun.* **11** 3650
[9] Hua X Y, Zeng Z M, Meng F B, Yao H X, Huang Z Y, Long X Y, Li Z H, Wang Y F, Wang Z Y, Wu T, Weng Z Y, Wang Y H, Liu Z, Xiang Z J and Chen X H 2024 *Nat. Phys.* **20** 957
[10] Ning Z F, Qian J H, Liu Y X, Chen F, Zhang M Z, Deng L W, Yuan X L, Ge Q Q, Jin H, Zhang G Q, Peng W, Qiao S, Mu G, Chen Y and Li W 2024 *Nano Lett.* **24** 7134
[11] Liu G Z, Qiu J, Jiang Y C, Zhao R and Gao J 2018 *Mater. Res. Express* **5** 046308
[12] Yang G, Kim Y, Jeon J, Lee M, Kim D, Kim S, Eom K and Lee H 2023 *Nano Lett.* **23** 6369
[13] Li D F, Lee K, Wang B Y, Osada M, Crossley S, Lee H R, Cui Y, Hikita Y and Hwang H Y 2019 *Nature* **572** 624
[14] Huang K and Han R Q 1988 *Solid State Physics* 1st Edn. (Beijing: Higher Education Press)
[15] Baroni S, de Gironcoli S, Dal Corso A and Giannozzi P 2001 *Rev. Mod. Phys.* **73** 515
[16] Kumar N, Najimu M O, Cho Y J, Gilliard-AbdulAziz K L, Nikolla E, Wu Z and Wachs I E 2025 *Chem. Rev.* **125** 8921
[17] Sobota J A, Teitelbaum S W and Huang Y, *et al.* 2023 *Phys. Rev. B* **107** 014305
[18] Shi R C, Li Q I, Xu X F, Han B, Zhu R X, Liu F C, Qi R S, Zhang X W, Du J L, Chen J, Yu D P, Zhu X T, Guo J D and Gao P 2024 *Nat. Commun.* **15** 3418
[19] Pentcheva R and Pickett W E 2006 *Phys. Rev. B* **74** 035112
[20] Lee H, Campbell N, Lee J, Asel T J, Paudel T R, Zhou H, Lee J W, Noesges B, Seo J, Park B, Brillson L J, Oh S H, Tsymbal E Y, Rzchowski M S and Eom C B 2018 *Nat. Mater.* **17** 231
[21] Zhang Z and Yates J T 2012 *Chem. Rev.* **112** 5520
[22] Cao Y, Chen S Y, Li Y D, Gao Y, Yang D H, Shen Y R and Liu W T 2016 *Sci. Adv.* **2** e1601162
[23] Zhang S Y, Wei T, Guan J Q, Zhu Q, Qin W, Wang W H, Zhang J D, Plummer E W, Zhu X T, Zhang Z Y and Guo J D 2019 *Phys. Rev. Lett.* **122** 066802
[24] Yang H B, Zhou Y N, Miao G Y, Rusz J, Yan X X, Guzman F, Xu X F, Xu X H, Aoki T, Zeiger P, Zhu X T, Wang W H, Guo J D, Wu R Q and Pan X Q 2024 *Nature* **635** 332
[25] Karmanenko S F, Belousov M V, Chakalov R A, Davydov V Y, Dedyk A I, Likholetov Y V, Njakshev K F, Pavlovskaya M V and Ter-Martirosyan L T 1994 *Supercond. Sci. Technol.* **7** 727
[26] Zhang M D, Shi R C, Wu R, Jiao X T, Shi M X, Liu J X, Wang Y B, Dong W F, Ding C, Qin T X, Liu H Y, Wang L L, Zhang Z Y, Gao P, Xue Q K and Xiong Q H 2025 *Phys. Rev. Lett.* **135** 126903
[27] Shen Y R 1989 *Nature* **337** 519
[28] Günter T, Rubano A, Paparo D, Lillienblum M, Marrucci L, Miletto Granozio F, Scotti Di Uccio U, Jany R, Richter C, Mannhart J and Fiebig M 2012 *Phys. Rev. B* **86** 235418
[29] Shen Y R 1984 *The Principles of Nonlinear Optics* (New York: Wiley-Interscience)
[30] Shen Y R 2016 *Fundamentals of Sum-Frequency Spectroscopy* (Cambridge: Cambridge University Press)
[31] Liu W T and Shen Y R 2008 *Phys. Rev. B* **78** 024302
[32] Liu X Y, Zhou T, Yuan Z, Ma C J, Lu F J, Liu T Y, Li J S, Wei S H, Cheng G L and Liu W T 2023 *Sci. Adv.* **9** eadg7037
[33] Gonzalez R J, Zallen R and Berger H 1997 *Phys. Rev. B* **55** 7014
[34] Dresselhaus M S, Dresselhaus G and Jorio A 2008 *Group Theory: Application to the Physics of Condensed Matter* (Berlin: Springer)
[35] Fujishima A, Zhang X and Tryk D A 2008 *Surf. Sci. Rep.* **63** 515
[36] Setvin M, Franchini C, Hao X, Schmid M, Janotti A, Kaltak M, Van de Walle C G, Kresse G and Diebold U 2014 *Phys. Rev. Lett.* **113** 086402
[37] Scheiber P, Fidler M, Dulub O, Schmid M, Diebold U, Hou W, Aschauer U and Selloni A 2012 *Phys. Rev. Lett.* **109** 136103
[38] Tilocca A and Selloni A 2004 *J. Phys. Chem. B* **108** 19314
[39] Tilocca A and Selloni A 2004 *J. Phys. Chem. B* **108** 4743
[40] Li Y D and Gao Y 2014 *Phys. Rev. Lett.* **112** 206101
[41] Liu X Y, Zhou T and Liu W T 2019 *J. Chem. Phys.* **150** 084701
[42] Guo N, Chen X Y, Yu T L, Fan Y, Zhang Q H, Lei M, Xu X F, Zhu X T, Guo J D, Gu L, Xu H C, Peng R and Feng D L 2024 *Nano Lett.* **24** 8587
[43] Fuchs R and Kliewer K L 1965 *Phys. Rev.* **140** A2076
[44] Lüth H 2015 *Solid Surfaces, Interfaces and Thin Films* 6th Edn. (Cham: Springer)
[45] Garcia A B S, Bispo-Jr A G, Lima S A M and Pires A M 2021 *Mater. Res. Bull.* **143** 111462
[46] Pauli S A, Leake S J, Delley B, Björck M, Schneider C W, Schlepütz C M, Martoccia D, Paetel S, Mannhart J and Willmott P R 2011 *Phys. Rev. Lett.* **106** 036101
[47] Zhou J, Asmara T C, Yang M, Sawatzky G A, Feng Y P and Rusydi A 2015 *Phys. Rev. B* **92** 125423
[48] Lee P W, Singh V N, Guo G Y, Liu H J, Lin J C, Chu Y H, Chen C H and Chu M W 2016 *Nat. Commun.* **7** 12773
[49] Savoia A, Paparo D, Perna P, Ristic Z, Salluzzo M, Granozio F M, di Uccio U S, Richter C, Thiel S, Mannhart J and Marrucci L 2009 *Phys. Rev. B* **80** 075110

[50] Min T, Choi W, Seo J, Han G, Song K, Ryu S, Lee H, Lee J, Eom K, Eom C, Jeong H Y, Kim Y, Lee J and Oh S H 2021 *Sci. Adv.* **7** eabe9053
[51] Asmara T C, Annadi A, Santoso I, Gogoi P K, Kotlov A, Omer H M, Motapothula M, Breese M B H, Rübhausen M, Venkatesan T, Ariando and Rusydi A 2014 *Nat. Commun.* **5** 3663
[52] Devreese J T and Alexandrov A S 2009 *Rep. Prog. Phys.* **72** 066501
[53] Wang Z, McKeown Walker S and Tamai A, *et al*. 2016 *Nat. Mater.* **15** 835
[54] Xie Y, Cao H Y, Zhou Y, Chen S Y, Xiang H J and Gong X G 2015 *Sci. Rep.* **5** 10011
[55] Ha M K, Xiao Q, Qin Z Y, Qiu D W, Shang L B, Liu X Y, Yan P, Ma C J, Liu D Q, Huang C Y, Chen Z L, Wang H Y, Duan C, Liao Z L, Liu W T, Gao Y, Cao K C, Du J F and Cheng G L 2025 *Natl. Sci. Rev.* **12** nwaf156
[56] Chen Y Z, Trier F and Wijnands T, *et al*. 2015 *Nat. Mater.* **14** 801
[57] Lee D H 2015 *Chin. Phys. B* **24** 117405
[58] Yan G S, Wu W Y, Wang Y F, Lan M D, Zhang J S, Liang X, Zhang Y, Yu W S, Wu Y H and Shen S P 2025 *Int. J. Mech. Sci.* **304** 110693
[59] Ellinger F, Shafiq M, Ahmad I, Reticcioli M and Franchini C 2023 *Phys. Rev. Mater.* **7** 064602
[60] Di Valentin C and Selloni A 2011 *J. Phys. Chem. Lett.* **2** 2223
[61] Sze S M and Ng K K 2007 *Physics of Semiconductor Devices* 3rd Edn. (Hoboken, NJ: John Wiley & Sons)
[62] Lytle F W 1964 *J. Appl. Phys.* **35** 2212
[63] Tufte O N and Chapman P W 1967 *Phys. Rev.* **155** 796
[64] Jin H, Lee K, Baek S, Kim J, Cheong B, Park B H, Yoon S, Suh B J, Kim C, Seo S S A and Lee S 2016 *Sci. Rep.* **6** 34295
[65] Luo L C, Li J L, Wang M W, Yang S, Wu J, Gao X Y, Li C C, Du W Y, Zhang L and Li F 2022 *Ceram. Int.* **48** 28438
[66] Rupprecht G and Bell R O 1964 *Phys. Rev.* **135** A748
[67] Gonella G and Dai H 2014 *Langmuir* **30** 2588
[68] Roke S 2009 *ChemPhysChem* **10** 1380
[69] Wang J, Bisson P J, Marmolejos J M and Shultz M J 2016 *J. Phys. Chem. Lett.* **7** 1945
[70] Yu C, Seki T, Chiang K, Tang F, Sun S, Bonn M and Nagata Y 2022 *J. Phys. Chem. B* **126** 6113
[71] Chen H L, Lian Y, Zhou T, Li H, Li J S, Liu X Y, Huang Y and Liu W T 2024 *Nanomaterials* **14** 1892